



Article

# Impact of Strain and Morphology on Magnetic Properties of Fe<sub>3</sub>O<sub>4</sub>/NiO Bilayers Grown on Nb:SrTiO<sub>3</sub>(001) and MgO(001)

Olga Kuschel<sup>1</sup>, Nico Pathé<sup>1</sup>, Tobias Schemme<sup>1</sup>, Kevin Ruwisch<sup>1</sup>, Jari Rodewald<sup>1</sup>, Ralph Buss<sup>1</sup>, Florian Bertram<sup>2</sup>, Timo Kuschel<sup>3</sup> , Karsten Kuepper<sup>1</sup> and Joachim Wollschläger<sup>1,\*</sup> 

<sup>1</sup> Department of Physics and Center of Physics and Chemistry of New Materials, Osnabrück University, 49076 Osnabrück, Germany; oschuckm@uos.de (O.K.); npathe@uos.de (N.P.); toschemm@uos.de (T.S.); kruwisch@uos.de (K.R.); jarodewa@uos.de (J.R.); rbuss@uos.de (R.B.); kkuepper@uos.de (K.K.)

<sup>2</sup> Deutsches Elektronen-Synchrotron (DESY), Photon Science, 22607 Hamburg, Germany; florian.bertram@desy.de

<sup>3</sup> Center for Spinelectronic Materials and Devices, Department of Physics, Bielefeld University, 33615 Bielefeld, Germany; tkuschel@physik.uni-bielefeld.de

\* Correspondence: jwollsch@uos.de; Tel.: +49-541-969-2651

Received: 5 June 2018; Accepted: 27 June 2018; Published: 30 June 2018



**Abstract:** We present a comparative study of the morphology and structural as well as magnetic properties of crystalline Fe<sub>3</sub>O<sub>4</sub>/NiO bilayers grown on both MgO(001) and SrTiO<sub>3</sub>(001) substrates by reactive molecular beam epitaxy. These structures were investigated by means of X-ray photoelectron spectroscopy, low-energy electron diffraction, X-ray reflectivity and diffraction, as well as vibrating sample magnetometry. While the lattice mismatch of NiO grown on MgO(001) was only 0.8%, it was exposed to a lateral lattice mismatch of −6.9% if grown on SrTiO<sub>3</sub>. In the case of Fe<sub>3</sub>O<sub>4</sub>, the misfit strain on MgO(001) and SrTiO<sub>3</sub>(001) amounted to 0.3% and −7.5%, respectively. To clarify the relaxation process of the bilayer system, the film thicknesses of the magnetite and nickel oxide films were varied between 5 and 20 nm. While NiO films were well ordered on both substrates, Fe<sub>3</sub>O<sub>4</sub> films grown on NiO/SrTiO<sub>3</sub> exhibited a higher surface roughness as well as lower structural ordering compared to films grown on NiO/MgO. Further, NiO films grew pseudomorphic in the investigated thickness range on MgO substrates without any indication of relaxation, whereas on SrTiO<sub>3</sub> the NiO films showed strong strain relaxation. Fe<sub>3</sub>O<sub>4</sub> films also exhibited strong relaxation, even for films of 5 nm thickness on both NiO/MgO and NiO/SrTiO<sub>3</sub>. The magnetite layers on both substrates showed a fourfold magnetic in-plane anisotropy with magnetic easy axes pointing in ⟨100⟩ directions. The coercive field was strongly enhanced for magnetite grown on NiO/SrTiO<sub>3</sub> due to the higher density of structural defects, compared to magnetite grown on NiO/MgO.

**Keywords:** magnetite; nickel oxide; strain relaxation; magnetic anisotropy

## 1. Introduction

Transition metal oxides are one of the most interesting material classes, providing a huge variety of structural, magnetic, and electronic properties ranging from metallic to insulating, from ferro- to antiferromagnetic, as well as ferroelectric states [1]. Especially, thin magnetite films (Fe<sub>3</sub>O<sub>4</sub>) have attracted intensive research interest in the last decade in the field of spintronics [2] and spin caloritronics [3,4]. Due to their anticipated half-metallic behavior with complete spin polarization at the Fermi level [5] and high (bulk) Curie temperature of 858 K [6], thin magnetite films are promising candidates for room temperature spintronic devices such as highly spin-polarized electrodes for magnetic tunneling junctions [7–9] or spin injectors [10]. Furthermore, multilayers of magnetite and

platinum show huge thermoelectric effects [11] based on the recently observed spin Seebeck effect in magnetite [12] pushing the development of more efficient thermoelectric nanodevices [13].

Magnetite crystallizes in the inverse spinel structure with a lattice constant of 8.3963 Å [6] at 300 K. At ~120 K it undergoes a metal–insulator transition (Verwey transition) [14] accompanied by a change from cubic to monoclinic crystal symmetry [15]. The reduction of the crystal symmetry leads to a spontaneous ferroelectric polarization, and thus to multiferroicity [16,17].

In order to control the relative magnetization alignment in magnetic tunnel junctions, exchange bias effects induced by additional antiferromagnetic layers are commonly used [18]. In the case of Fe<sub>3</sub>O<sub>4</sub> tunnel junctions, the antiferromagnetic NiO is a good candidate due to its small lattice mismatch of only 0.5% and a high Néel temperature of 523 K [19].

Nickel oxide is an insulating material with a high thermal stability. It crystallizes in a rock salt structure with a lattice constant of 4.1769 Å [20] at 300 K. It was recently shown that NiO can act as a spin current amplifier in spin Seebeck experiments, and can additionally be a spin current generator when a thermal gradient is applied [21–24], making NiO a key material for thermoelectric devices. Further, the latest studies report on a temperature-dependent sign change in the spin hall magnetoresistance for nickel oxide on ferromagnetic insulator [25,26]. Thus, there is a possibility to use it as a spin filter.

Previous works [27–33] have focused on the characterization of magnetite and nickel oxide films grown on MgO substrates because of the small lattice mismatch of 0.3% and 0.8%, respectively. However, it has been demonstrated that the electronic and magnetic properties of magnetite films can be modified using SrTiO<sub>3</sub> substrates [34–36], despite the large lattice mismatch of –7.5%. One advantage of using SrTiO<sub>3</sub> substrates is the possibility of doping and, thus, a tunable conductivity providing either an insulating or metallic substrate which can be used as a bottom electrode in capacitor-like structures [17]. Furthermore, Fe<sub>3</sub>O<sub>4</sub>/NiO bilayers grown on SrTiO<sub>3</sub> can be used to synthesize Ni<sub>x</sub>Fe<sub>3–x</sub>O<sub>4</sub> thin films by thermally induced interdiffusion with tunable magnetic and electric properties [37].

To date, most studies concerning NiO films on SrTiO<sub>3</sub> have been limited to a coarse analysis of the growth [38,39], while a thorough structural characterisation is seldom reported [40]. In the case of Fe<sub>3</sub>O<sub>4</sub>/NiO bilayers on both substrates, there are a number of works on electronic structure, interfacial coupling, and magnetic characterization [41–44], whereas to the best of our knowledge there are no detailed structural studies for these bilayers on SrTiO<sub>3</sub>. However, the magnetic and transport characteristics of such films are sensitive to structural variations, number of defects, or stoichiometric deviations, and can be affected by the strain between film and substrate [36]. Therefore, in this work, a comprehensive structural characterization of Fe<sub>3</sub>O<sub>4</sub>/NiO bilayers of different thicknesses grown on Nb-doped SrTiO<sub>3</sub>(001) and for comparison on MgO(001) is presented. Additionally, these results are correlated with magnetic properties (e.g., magnetocrystalline anisotropy).

Directly after deposition, the stoichiometry in the near-surface region and the surface structure of each layer was determined in situ using X-ray photoelectron spectroscopy (XPS) and low-energy electron diffraction (LEED), respectively. The bulk structure was investigated ex situ by X-ray reflectivity (XRR) and synchrotron radiation X-ray diffraction (SR-XRD) measurements and analyzed within kinematic diffraction theory. Further, angle-dependent hysteresis loops were measured via vibrating sample magnetometry (VSM).

## 2. Materials and Methods

Preparation and in situ characterization of the thin oxide films were carried out in an interconnected ultrahigh vacuum (UHV) system at a base pressure of 10<sup>–8</sup> mbar in the deposition chamber and 10<sup>–10</sup> mbar in the analysis chamber. Epitaxial Fe<sub>3</sub>O<sub>4</sub>/NiO ultra-thin bilayer systems with thicknesses between 5 nm and 20 nm were grown via reactive molecular beam epitaxy (RMBE) on 0.05% Nb-doped SrTiO<sub>3</sub>(001) or on MgO(001) single crystalline substrates. Prior to deposition, the substrates were annealed at 400 °C in 1 × 10<sup>–4</sup> mbar O<sub>2</sub> atmosphere for 1 h in order to remove

carbon contamination and get well-defined surfaces. Subsequently, nickel oxide and magnetite films were deposited by thermal evaporation from pure metal rods in  $1 \times 10^{-5}$  mbar and  $5 \times 10^{-6}$  mbar oxygen atmosphere, respectively. Deposition was performed at 250 °C substrate temperature using deposition rates of 0.01 nm/s for nickel oxide films and 0.25 nm/s for magnetite films, as controlled by a quartz microbalance adjacent to the evaporation source. The resulting film thicknesses were determined later on ex situ by XRR (Panalytical, Philips X'Pert Pro, Almelo, The Netherlands) Crystal surface quality and near-surface stoichiometry were controlled in situ after each preparation step by LEED (ErLEED 150, SPECS, Berlin, Germany) and XPS (SPECS, Berlin, Germany) using an Al  $K_{\alpha}$  ( $h\nu = 1486.6$  eV) radiation source and a Phoibos HSA 150 hemispherical analyzer.

After transport under ambient conditions, XRR and XRD experiments were carried out ex situ for structural characterization of the films. XRR measurements were performed in  $\theta$ - $2\theta$  geometry using a lab based diffractometer equipped with a Cu  $K_{\alpha}$  anode. An in-house developed fitting tool based on the Parratt algorithm [45] using Névo-Croce [46] roughness profiles was applied for the analysis of the XRR curves. For XRD synchrotron based radiation sources at the MaXLab beamline I811 (MaXLab, Lund, Sweden) and at the Swiss Light Source beamline X04SA (Paul Scherrer Institute, Villigen, Switzerland) were used. Both beamlines are equipped with (2S + 3D) type diffractometers and Pilatus pixel area detectors for data collection. The XRD data were recorded in  $\theta$ - $2\theta$  geometry at an energy of 12.4 keV and analyzed within the kinematic diffraction theory [47] that is implemented in our in-house developed fitting tool.

In addition, magnetization curves were measured at room temperature for several in-plane directions of the samples by varying the magnetic field  $\mu_0 H$  between  $-300$  mT and  $+300$  mT, using a VSM (Lakeshore, Model 7407, Westerville, OH, USA). The magnetization loops were corrected by subtracting the diamagnetic contribution from the substrates.

### 3. Results

#### 3.1. LEED/XPS

Figure 1a,d presents the LEED patterns of the cleaned MgO(001) and SrTiO<sub>3</sub>(001) surfaces, respectively. All as-prepared NiO and Fe<sub>3</sub>O<sub>4</sub> films showed similar LEED patterns on the respective substrate for all investigated thicknesses ranging from 5 nm to 20 nm. Thus, only patterns of a  $\sim 20$  nm Fe<sub>3</sub>O<sub>4</sub> and a  $\sim 10$  nm NiO film on MgO and SrTiO<sub>3</sub> are shown as examples in Figure 1. The intensity variations in all recorded patterns were due to dynamical scattering for electron diffraction, and will not be considered further. Instead, we focus on the symmetry of the diffracted pattern and the sharpness of the diffraction spots.

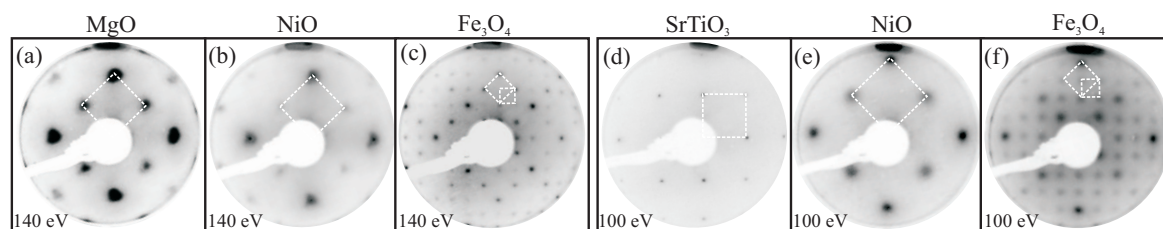


**Figure 1.** Low-energy electron diffraction (LEED) pattern recorded at 140 eV for (a) pure MgO(001) surface; (b) 11.9 nm NiO film on MgO(001); and (c) 21.5 nm Fe<sub>3</sub>O<sub>4</sub> on NiO/MgO(001). The LEED pattern taken at 100 eV of a pure SrTiO<sub>3</sub> surface, a 10.4 nm NiO film on SrTiO<sub>3</sub>(001), and 20.7 nm Fe<sub>3</sub>O<sub>4</sub> on NiO/SrTiO<sub>3</sub>(001) are depicted in (d–f), respectively. The larger white squares indicate the (1 × 1) structure of the reciprocal unit cell of the respective surfaces, while the smaller white squares in (c) and (f) indicate the  $(\sqrt{2} \times \sqrt{2})R45^\circ$  superstructure unit cell of magnetite.

Clear (1 × 1) structures corresponding to the square unit cells of MgO(001) and SrTiO<sub>3</sub>(001) surfaces could be seen (cf. Figure 1a,d). Due to the rock salt structure of MgO, the reciprocal unit vectors of

the MgO(001) surface point in [110] and  $[\bar{1}10]$  directions, forming a quadratic reciprocal unit cell. The reciprocal unit vectors of the (001) surface of the perovskite SrTiO<sub>3</sub> point in [100] and [010] directions, also forming a quadratic unit cell. Consequently, the reciprocal surface unit vectors of MgO(001) are  $\sim\sqrt{2}$  times larger than those of SrTiO<sub>3</sub>(001).

In diffraction patterns, a random arrangement of point defects leads to an increased background, while line defects (e.g., domain boundaries) result in a broadening of the diffraction spots [48]. To obtain not only qualitative but also quantitative information on the defect density, the full width of half maximum (FWHM) of the diffraction spots was determined at 140 eV, taking into account the instrumental broadening of the LEED instrument.

The SrTiO<sub>3</sub> pattern exhibited sharp and intense diffraction spots. Analysis of the FWHM of the (11) diffraction peaks yielded a line defect density of  $(0.11 \pm 0.02) \text{ nm}^{-2}$ . In contrast, the spots of the MgO substrate were broadened due to charging effects. Thus, it was not possible to determine a value for the defect density of the substrate here. The diffuse background was quite low in both patterns, pointing to clean surfaces and negligible point defects. Additionally, XPS measurements of both substrates showed no carbon contamination, indicating chemically clean surfaces.

After the deposition of NiO, the LEED patterns also exhibited a  $(1 \times 1)$  structure related to the square symmetry of the NiO(001) surface for both substrates (cf. Figure 1b,e). As mentioned above, due to the rock salt structure, the reciprocal unit vectors of the NiO(001) surface point in [110] and  $[\bar{1}10]$  directions and are consequently  $\sim\sqrt{2}$  times larger than the surface unit cell of SrTiO<sub>3</sub> in reciprocal space. Due to the very similar lattice constants of NiO(001) and MgO(001), the diffraction spots were located at almost identical positions. A broadening of the diffraction spots compared to the pattern of the SrTiO<sub>3</sub> substrate was clearly visible, indicating an increase of the defect density. Analyzing the FWHM of the (10) surface diffraction spots, we obtained densities of line defects of  $(0.8 \pm 0.1) \text{ nm}^{-2}$  and  $(1.1 \pm 0.2) \text{ nm}^{-2}$  for the NiO/MgO and NiO/SrTiO<sub>3</sub>, respectively. The slightly larger broadening of the diffraction spots for NiO/SrTiO<sub>3</sub> compared to the diffraction spots of the NiO/MgO surface can be related to the formation of more structural defects (e.g., domain boundaries), induced by the higher lattice misfit of NiO(001) on SrTiO<sub>3</sub>(001). Additionally, both patterns showed a negligible background intensity of the NiO(001) surface, pointing to a small amount of point defects.

The LEED images of Fe<sub>3</sub>O<sub>4</sub> obtained after deposition on NiO/MgO(001) and NiO/SrTiO<sub>3</sub>(001) showed similar diffraction patterns with a square symmetry (cf. Figure 1c,f). Clear diffraction spots with half-peak distance compared to the NiO(001) surface indicated an approximately doubled lattice constant in real space due to the almost-doubled cubic lattice constant of Fe<sub>3</sub>O<sub>4</sub> compared to the other oxides used here. Furthermore, an additional  $(\sqrt{2} \times \sqrt{2})R45^\circ$  superstructure appeared, which is characteristic for a well-ordered magnetite surface [49–52]. This superstructure is not observed for maghemite (Fe<sub>2</sub>O<sub>3</sub>), which has a very similar surface lattice constant. Therefore, we assume the formation of well-ordered stoichiometric magnetite films. However, the diffraction spots of the magnetite film grown on NiO/MgO were sharper than for the growth on NiO/SrTiO<sub>3</sub>, indicating a better ordering and less domain boundaries. For the density of line defects of the Fe<sub>3</sub>O<sub>4</sub> films, values of  $(1.3 \pm 0.2) \text{ nm}^{-2}$  and  $(0.14 \pm 0.02) \text{ nm}^{-2}$  were obtained for the growth on NiO/SrTiO<sub>3</sub>(001) and NiO/MgO(001), respectively, analyzing the FWHM of the (20) surface diffraction spots.

In summary, the LEED patterns of the Fe<sub>3</sub>O<sub>4</sub>/NiO bilayer systems confirmed a crystalline cube-on-cube growth of both NiO and Fe<sub>3</sub>O<sub>4</sub> films on MgO(001), as well as on SrTiO<sub>3</sub>(001). The films grown on MgO substrates exhibited a higher crystalline quality and less surface defects compared to the bilayers grown on SrTiO<sub>3</sub>.

XPS measurements were made directly after deposition of the films to determine the stoichiometry and the valence state of the cation species. Figure 2a shows the XP spectra of the Ni 2p region after the deposition of nickel oxide and before the deposition of iron oxide. All spectra of the Ni 2p core level revealed Ni 2p<sub>3/2</sub> and Ni 2p<sub>1/2</sub> peaks at binding energies of 854.6 eV and 872.5 eV, respectively, and two intense satellite structures at about 7 eV higher binding energies. Since these values agree well with the binding energies reported in the literature for a Ni<sup>2+</sup> valence state in NiO stoichiometry [53,54],

we assume that the oxide films were stoichiometric and had negligible point defects (e.g., oxygen vacancies). Additionally, there was a shoulder  $\sim 1.5$  eV above the Ni 2p<sub>3/2</sub> peak, which has been reported to be typical for NiO [55,56]. Thus, the shape of all spectra was comparable to that of NiO bulk crystal [54,57,58].

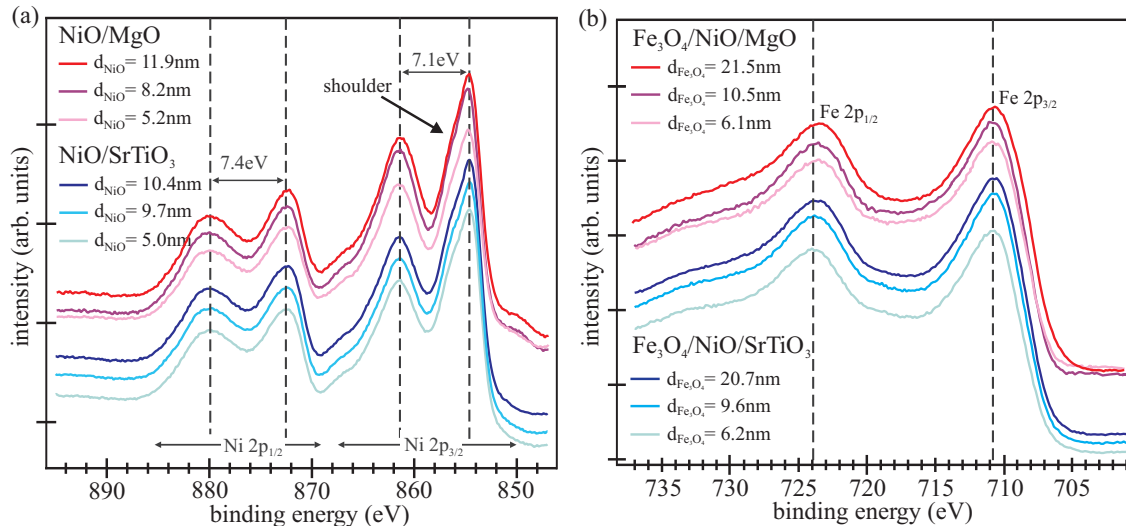


**Figure 2.** X-ray photoelectron spectra of (a) Ni 2p region for the as-prepared NiO films on MgO(001) and SrTiO<sub>3</sub>; (b) Fe 2p region for the as-prepared Fe<sub>3</sub>O<sub>4</sub> films on NiO/MgO(001) and NiO/SrTiO<sub>3</sub>.

The Fe 2p photoelectron spectra of the iron oxide films as prepared on top of the NiO films are presented in Figure 2b. From the position and shape of the Fe 2p peaks, one can obtain information about the iron oxidation state and the stoichiometry. All recorded spectra exhibited the same shape, with main peaks located at binding energies of 710.6 eV and 723.6 eV for Fe 2p<sub>3/2</sub> and Fe 2p<sub>1/2</sub>, respectively. These binding energies of the core levels correspond to well-known values of Fe<sub>3</sub>O<sub>4</sub> from the literature [59]. Additionally, in contrast to wüstite (FeO) and maghemite (Fe<sub>2</sub>O<sub>3</sub>), no apparent charge transfer satellites can be observed between the two main peaks due to their overlap [59,60]. Consequently, the shape and binding energies of the Fe 2p spectra confirmed a mixed Fe<sup>2+</sup>/Fe<sup>3+</sup> valence and pointed to a Fe<sub>3</sub>O<sub>4</sub> stoichiometry for all prepared iron oxide films. Thus, both XPS and LEED measurements demonstrated that the bilayer structures on both kind of substrates consisted of crystalline stoichiometric NiO and Fe<sub>3</sub>O<sub>4</sub> films.

### 3.2. XRR/XRD

XRR and XRD experiments were performed *ex situ* to determine the structural parameters of the bilayers (e.g., film thicknesses and vertical lattice distances). Figure 3a,b shows the measured reflectivity curves and the corresponding calculated reflectivity curves after optimizing the structural parameters. In addition, the obtained thicknesses of all studied bilayers are presented. Clear intensity oscillations with beating effects were visible for all samples, indicating double-layer structures and flat homogenous films with small interface and surface roughness.

The applied calculation model consists of a layer of iron oxide on top of a nickel oxide layer on MgO or SrTiO<sub>3</sub> substrate. All fitted curves agreed excellently with the experimental data using literature values for the dispersion  $\delta_{\text{Fe}_3\text{O}_4} = 1.53 \times 10^{-5}$  and  $\delta_{\text{NiO}} = 1.89 \times 10^{-5}$  [61]. This indicates a small defect density (e.g., oxygen vacancies), which is in accordance with the XPS results.

Additionally, the roughnesses of the films were determined and are presented in Figure 3c. Here, all films featured an increase of the surface and interface roughness with increasing film thickness. This effect can be attributed to kinetic roughening of the films during growth and to the progressing relaxation process [62]. The nickel oxide films exhibited similar roughnesses of  $\sigma_{\text{NiO}} = 2.5\text{--}3.5$  Å on

both substrates, with a small increase for thicker films. The roughness of the  $\text{Fe}_3\text{O}_4$  on NiO/MgO increased more drastically, while the magnetite films deposited on NiO/SrTiO<sub>3</sub> showed nearly constant roughness with initially almost doubled values compared to the magnetite films on NiO/MgO. This behavior is likely caused by high lattice misfit and the resulting relaxation process. This is in accordance with the broadened diffraction spots of the  $\text{Fe}_3\text{O}_4$  films on NiO/SrTiO<sub>3</sub> observed in the LEED pattern (cf. Figure 1).

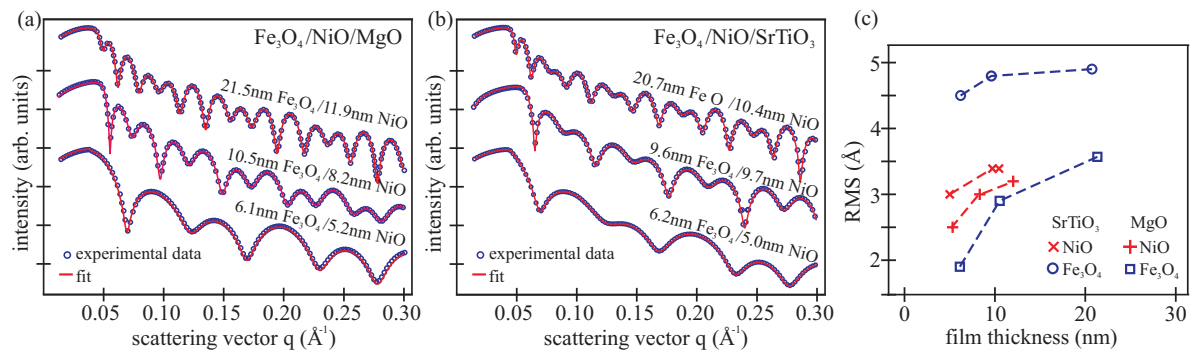


**Figure 3.** X-ray reflectivity (XRR) measurements and the calculated intensities of the bilayers on (a) MgO and (b) SrTiO<sub>3</sub> substrates; (c)  $\text{Fe}_3\text{O}_4$  surface and  $\text{Fe}_3\text{O}_4/\text{NiO}$  interface roughnesses obtained from the XRR measurements.

Figure 4a,b presents the SR-XRD measurements of the (00L) crystal truncation rod (CTR) compared to intensities calculated by kinematic diffraction theory of the  $\text{Fe}_3\text{O}_4/\text{NiO}$  bilayers on MgO(001) and SrTiO<sub>3</sub>(001), respectively. Here, the bulk nomenclature of the reciprocal space was used, where  $L = c K_{\perp} / (2\pi)$  in reciprocal lattice units (r.l.u.) denotes the vertical scattering vector  $K_{\perp}$  scaled to the Bragg condition  $2\pi/c$  ( $c_{\text{MgO}} = 4.2117 \text{ \AA}$ ,  $c_{\text{SrTiO}_3} = 3.905 \text{ \AA}$ ). The diffraction data revealed an epitaxial (001)-oriented growth of NiO and  $\text{Fe}_3\text{O}_4$  on both substrates. Due to the almost-doubled lattice constant of magnetite compared to both MgO and NiO and the resulting lateral tensile strain, the (004)<sub>S</sub> spinel reflection was located at higher L values compared to MgO and close to the (002)<sub>R</sub> bulk reflection of a rock salt structure. On SrTiO<sub>3</sub>, both nickel oxide and magnetite exhibited a large lattice misfit and were laterally compressively strained. Thus, the (004)<sub>S</sub> reflection of magnetite and (002)<sub>R</sub> reflection of NiO were at lower L values compared to SrTiO<sub>3</sub> and were well separated from the (002)<sub>P</sub> perovskite reflection of SrTiO<sub>3</sub>. Here, the indexes R, S, and P indicate bulk indexing for rock salt, spinel, and perovskite types, respectively.

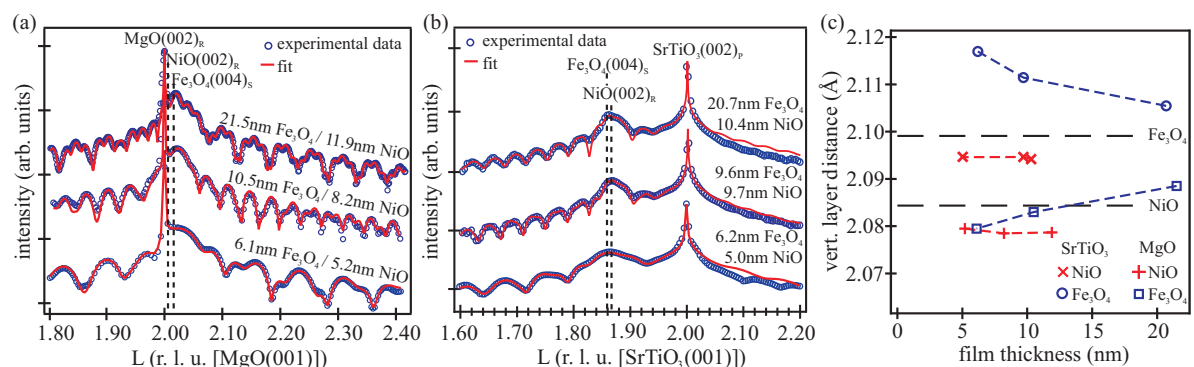


**Figure 4.** X-ray diffraction (XRD) measurement along the (00L) crystal truncation rod (CTR) (a) of the  $\text{Fe}_3\text{O}_4/\text{NiO}/\text{MgO}$  samples and (b) of the  $\text{Fe}_3\text{O}_4/\text{NiO}$  bilayers on SrTiO<sub>3</sub>. The calculated intensity distribution using the kinematic approximation is shown in red. (c) Vertical layer distance of nickel oxide and magnetite grown on MgO(001) and SrTiO<sub>3</sub>(001), dependent on the film thickness. The dashed lines denote the fully relaxed bulk values of magnetite and nickel oxide.

For all bilayers grown on MgO, the measurements showed a sharp peak at  $L = 2$  originating from the diffraction at the MgO substrate lattice (cf. Figure 4a). Additionally, broad and rather intense features located at  $L \sim 2.02$  accompanied by strong Laue oscillations were visible due to the finite thickness of the iron and nickel oxide films. The well-pronounced intensity oscillations with two superposed partial oscillations clearly showed a periodicity of two layers of different thickness, indicating a high crystalline ordering and homogenous thicknesses of both films—magnetite and nickel oxide. This is in accordance with the results seen in the XRR measurements.

In the case of bilayers grown on SrTiO<sub>3</sub>, the (00L) rod also showed a sharp substrate peak at  $L = 2$  and Laue oscillations due to crystalline magnetite and nickel oxide films (cf. Figure 4b). Here, the Bragg peaks originating from the iron and nickel oxide were located at  $L \sim 1.86$  and were broadened due to the finite film thicknesses. Upon closer inspection, the Laue oscillations also showed a periodicity of two layers, whereby the damping of the oscillation originating from the magnetite surface increased with increasing magnetite thickness due to increasing roughness (cf. Figure 3c). This result agrees well with LEED and XRR results shown above.

Due to the small lattice mismatch between Fe<sub>3</sub>O<sub>4</sub> and NiO, a separation of the Bragg peaks originating from the respective film is not visible by eye. Complete data analysis using kinematic diffraction theory was performed to obtain the vertical layer distance of the respective oxide film. Within the calculation, the atomic form factors of oxygen, nickel, and iron atoms arranged in a bulk structure were kept constant while the vertical size of the unit cell was varied. Interface roughness was modeled with a Gaussian variation of the height as implemented for XRR by the Névot–Croce model [46]. The applied models consist of a homogenous Fe<sub>3</sub>O<sub>4</sub>/NiO bilayer on top of the respective substrate. This structural model involving the number of layers coincides with the layer model and the film thicknesses obtained from XRR calculations. The obtained vertical layer distances ( $c_{\text{NiO}}/2$  for NiO and  $c_{\text{Fe}_3\text{O}_4}/4$  for Fe<sub>3</sub>O<sub>4</sub>) are shown in Figure 4c.

The dashed lines mark the bulk values of the magnetite and nickel oxide. Due to the larger unit cell of MgO(001), pseudomorphic growth of NiO on MgO resulted in an expansion of the NiO unit cell in the lateral direction, and thus a vertical compression, and consequently a smaller vertical lattice distance. Exactly the opposite was expected in the case of NiO grown on SrTiO<sub>3</sub>(001), due to the smaller bulk unit cell of SrTiO<sub>3</sub> compared to NiO. Thus, the vertical lattice distance of NiO was larger than the bulk value, as observed in the experiment.

For the NiO layers on MgO, the vertical layer distance exhibited a compressive strain (2.078 Å) due to lateral tension, and showed no dependence on the NiO thickness in the investigated range (cf. Figure 4c). In the case of bilayers grown on SrTiO<sub>3</sub>, the vertical lattice distance of NiO (2.095 Å) pointed to tensile strain as a result of the lateral compression. Further, there was no dependence on the NiO thickness.

However, the situation was different for the relaxation of the magnetite films. Due to pseudomorphic growth of NiO on MgO, the vertical layer distance of Fe<sub>3</sub>O<sub>4</sub> grown on top of NiO/MgO was also slightly compressively strained but relaxed to higher values with increasing magnetite thickness. Its value relaxed from 2.0795 Å for the 6.1 nm thick magnetite film to 2.0885 Å for the thickest magnetite film. A strong relaxation with increasing film thickness of the magnetite could also be seen for magnetite films grown on NiO/SrTiO<sub>3</sub>. The vertical lattice distance of Fe<sub>3</sub>O<sub>4</sub> on NiO/SrTiO<sub>3</sub> was exposed to heavy tensile strain and decreased rapidly from 2.117 Å for the thinnest film to 2.106 Å for the 20.7 nm thick magnetite film.

### 3.3. VSM

As an example, the magnetic properties of the two thickest magnetite films on NiO/MgO and NiO/SrTiO<sub>3</sub> were studied by means of VSM. The magnetization curves were measured for different azimuthal sample directions  $\alpha$  between the substrate [100] direction and the applied magnetic field. Figure 5a,b shows the magnetic moment per f.u. (formula unit) as a function of the magnetic field for the bilayers on MgO and SrTiO<sub>3</sub>, respectively, for two different directions of the external magnetic field.

For both samples, a typical ferro(i)magnetic behavior was observed. Here, the red curves recorded with the magnetic field applied in the [010] direction of the substrates represent magnetic easy axes with a high magnetic remanence and coercive fields. The blue curves recorded with the magnetic field applied in the [110] direction exhibit the magnetic behavior of a magnetic hard axis due to a lower strength of the coercive field and a smaller magnetic remanence. However, from magnetic saturation to magnetic remanence, neither investigated sample was in a monodomain state. This can also be concluded from the squareness (magnetic remanence value divided by the saturation magnetization) for the field loop of the magnetic easy direction which is below one. This effect is probably originated in the presence of antiphase boundaries that pin the magnetic moments in different directions and, thus, support multidomain states rather than monodomain states, even for the case of having the magnetization aligned in the magnetic easy direction.

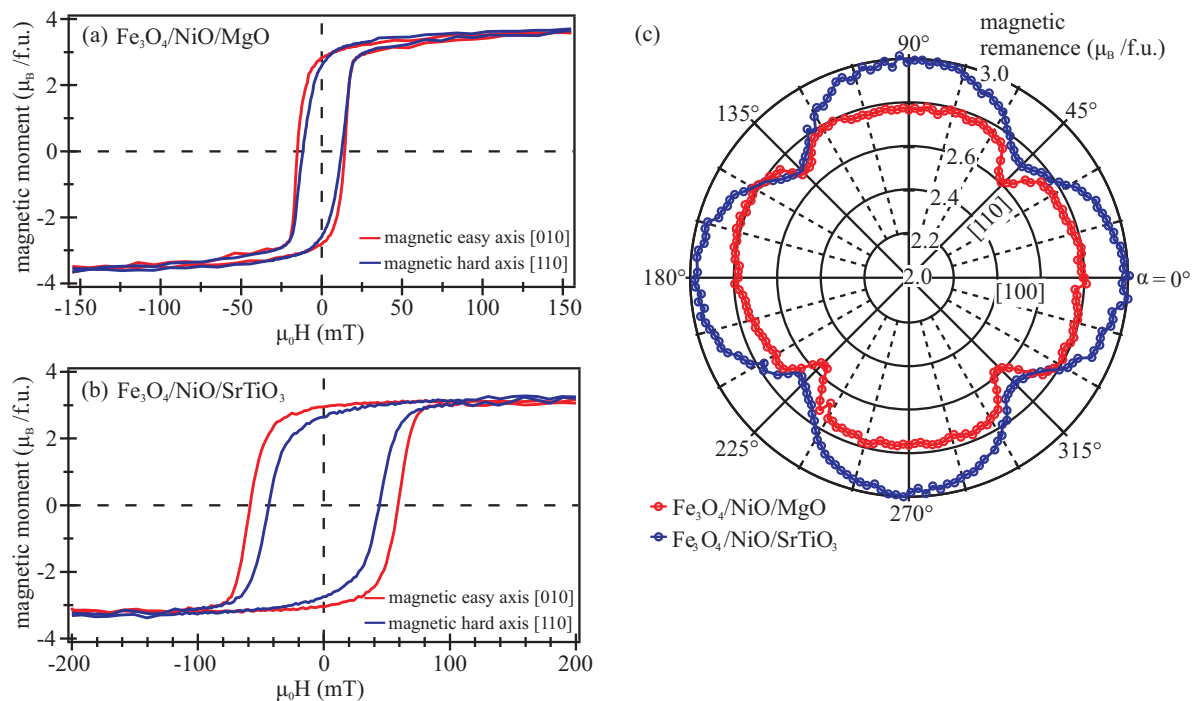


**Figure 5.** Vibrating sample magnetometry (VSM) magnetization curves of magnetic easy and hard directions for (a) 21.5 nm-thick Fe<sub>3</sub>O<sub>4</sub> film on NiO/MgO and (b) 20.7 nm-thick Fe<sub>3</sub>O<sub>4</sub> film on NiO/SrTiO<sub>3</sub>. (c) Polar plot of the magnetic remanence depending on the azimuthal sample angle  $\alpha$  of a 21.5 nm-thick Fe<sub>3</sub>O<sub>4</sub> film on NiO/MgO (red) and 20.7 nm-thick Fe<sub>3</sub>O<sub>4</sub> film on NiO/SrTiO<sub>3</sub> (blue).

The Fe<sub>3</sub>O<sub>4</sub> film on NiO/SrTiO<sub>3</sub> showed an enhanced coercive field compared to the magnetite film grown on NiO/MgO. One possible reason could be a higher density of grain boundaries due to the relaxation process, which supports pinned multidomain states that need larger magnetic fields to be switched. This is consistent with the weaker structural quality (e.g., high roughness, broad diffraction peaks) seen in the LEED, XRR, and XRD measurements. Further, the saturation magnetization of the Fe<sub>3</sub>O<sub>4</sub> film grown on NiO/MgO amounted to  $(3.7 \pm 0.3) \mu_B/f.u.$ , and was rather close to the literature value of  $4.07 \mu_B/f.u.$  [5,63]. In contrast, magnetite on NiO/SrTiO<sub>3</sub> showed a lower magnetic moment of  $(3.3 \pm 0.3) \mu_B/f.u.$ , which may result from the antiferromagnetic coupling in the vicinity of anti-phase domain boundaries (APBs) [64].

The remanent magnetization as a function of azimuthal sample angle  $\alpha$  is shown in Figure 5c for both investigated samples. The maxima of the magnetic remanence pointed in  $\langle 100 \rangle$  directions for both Fe<sub>3</sub>O<sub>4</sub> films on NiO/MgO and NiO/SrTiO<sub>3</sub>, indicating the magnetic easy directions. Consequently, the magnetic hard axes were located in  $\langle 110 \rangle$  directions.



#### 4. Discussion

XPS measurements taken directly after deposition revealed stoichiometric Fe<sub>3</sub>O<sub>4</sub> and NiO on both substrates, independent of the film thicknesses. Due to the limited mean free path of the electrons, only the near-surface region (~5 nm) of the layers could be characterized. No evidence for the formation of non-stoichiometric magnetite was observed in this region. Pilard et al. found a 1.5 nm-thick NiFe<sub>2</sub>O<sub>4</sub> interfacial layer after depositing NiO above 610 °C on Fe<sub>3</sub>O<sub>4</sub> [41]. Within the XPS measurements presented here, the interfacial region could be detected only for the thinnest magnetite films, showing spectral shape and binding energies typical for Ni<sup>2+</sup> in NiO stoichiometry. Thus, there was no evidence for the formation of NiFe<sub>2</sub>O<sub>4</sub>, due to the lower growth temperature.

Hard X-ray photoelectron spectroscopy (HAXPES) and X-ray magnetic circular dichroism (XMCD) measurements [42] of the same samples recorded after transport under ambient conditions showed small traces of Fe<sup>3+</sup> excess on the surface of the bilayers grown on SrTiO<sub>3</sub>. However, in deeper layers and at the interface, the presence of stoichiometric NiO and Fe<sub>3</sub>O<sub>4</sub> was confirmed, excluding the formation of NiFe<sub>2</sub>O<sub>4</sub> clusters or any interfacial layer also for thicker Fe<sub>3</sub>O<sub>4</sub> films [42]. Consequently, very thin magnetite films tend to form maghemite at the surface after exposure to ambient air whereas thicker films seem to be more stable, as reported previously by Fleischer et al. [65]. Since in situ XPS and LEED measurements taken after preparation under UHV conditions showed no evidence for maghemite, a capping layer deposited directly after growth could prevent the possible oxidation process in the upper layers.

In situ LEED measurements also verified the Fe<sub>3</sub>O<sub>4</sub> stoichiometry of the iron oxide film showing the typical ( $\sqrt{2} \times \sqrt{2}$ )R45° superstructure of the magnetite surface for all investigated films. Further, NiO films on both substrates exhibited the expected (1 × 1) pattern due to the rock salt crystal structure. The diffraction spots of the magnetite and NiO films grown on SrTiO<sub>3</sub> were slightly broadened compared to the films grown on MgO, indicating the formation of more surface defects due to the high lattice misfit. Surface roughnesses obtained from the XRR analysis exhibited higher values for all films grown on SrTiO<sub>3</sub>. While the roughness of the nickel oxide films deposited on SrTiO<sub>3</sub> was only about 0.5 Å higher than after deposition on MgO, the magnetite films on NiO/SrTiO<sub>3</sub> initially showed almost doubled values compared to the magnetite films on NiO/MgO. This result is consistent with the higher value for the defect density of Fe<sub>3</sub>O<sub>4</sub>/NiO/SrTiO<sub>3</sub> obtained from the LEED pattern analysis. Nevertheless, the XRR measurements provided distinct intensity oscillations, indicating double layer structures and homogenous film thicknesses. Thus, the two layers did not intermix during the deposition process.

The entire structure of the samples was investigated by XRD measurements of the specular CTR. For all samples, the thickness determined by XRR agreed well with the number of layers obtained from XRD analysis, where distinct Laue oscillations were observed. The strong intensity oscillations revealed crystalline and well-ordered nickel oxide and magnetite films with homogeneous thicknesses on both substrates.

The vertical layer distances of all NiO films showed no dependence on the thickness in the investigated range. However, NiO and Fe<sub>3</sub>O<sub>4</sub> films grown on MgO exhibited a vertical compressive strain while NiO and Fe<sub>3</sub>O<sub>4</sub> films on SrTiO<sub>3</sub> showed vertical tensile strain due to lattice matching at the interface. Based on elastic theory for continuum, the vertical lattice constant *c* for homogenous tetragonally (in-plane) distorted films is related to the lateral lattice constant *a* via [23]

$$\frac{\Delta c}{c} = \frac{2\nu}{\nu - 1} \frac{\Delta a}{a} \quad (1)$$

For the calculation of the vertical layer distance for a completely strained film,  $\Delta a$  from pseudomorphic growth was used. Assuming a Poisson number of  $\nu = 0.21$  for NiO [20], the vertical layer distance of pseudomorphic nickel oxide on MgO was calculated to be 2.079 Å. Hence, the NiO films grown on MgO were fully strained as clarified by Figure 6 where lateral distances of (100) planes are presented.

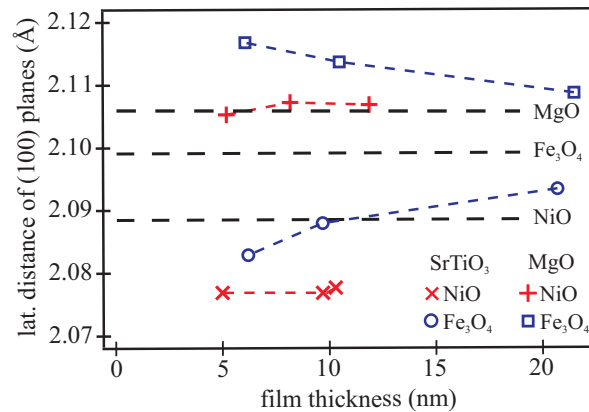


**Figure 6.** Lateral distance of (100) planes of all prepared magnetite and nickel oxide films calculated using Equation (1) and the vertical layer distances obtained from XRD analysis. The dashed lines denote the fully relaxed bulk values of MgO, Fe<sub>3</sub>O<sub>4</sub>, and NiO.

Above a critical thickness  $d_c$ , this strain should reduce rapidly due to the stable formation of dislocations. Following the model of Matthews and Blakeslee [66], the critical thickness  $d_c$ , at which the generation of misfit dislocation will begin, can be calculated by the formula

$$\frac{d_c}{b} = \frac{(1 - \nu \cos^2 \alpha) \left( \ln \left( \frac{d_c}{b} \right) + 1 \right)}{2 \pi f (1 + \nu) \cos(\lambda)}. \quad (2)$$

Here,  $b$  is the magnitude of the Burgers vector,  $f$  is the lattice mismatch,  $\nu$  is the Poisson ratio,  $\alpha = 90^\circ$  is the angle between the Burgers vector and the dislocation line, and  $\lambda = 45^\circ$  is the angle between the Burgers vector and the direction both normal to the dislocation line and within the plane of the interface. For NiO films on MgO(001), the critical thickness was determined to 39 nm. Since the studied films were below the critical thickness, the absence of strain relaxation is in good agreement with this model. Similar results were also observed by Schemme et al. [33] for NiO films of different thicknesses up to 34 nm grown on MgO(001). The experimental data of James et al. [20] showed a strain relaxation above  $\sim 40$  nm, which is consistent with our observations and confirms Equation (2).

Despite the large misfit of -6.9% between NiO and SrTiO<sub>3</sub>, the XRD curves of all studied films also featured distinct Laue oscillations, pointing to a good crystalline ordering. Assuming a complete lattice matching at the interface, we calculated a vertical lattice distance of 2.161 Å for fully strained NiO films on SrTiO<sub>3</sub> (Equation (1)), while we observed a film thickness independent value of 2.095 Å. The resulting lateral distances of the (100) planes calculated by Equation (1) of all investigated nickel oxide and magnetite films are presented in Figure 6. Thus, for the NiO films grown on SrTiO<sub>3</sub>, the remaining lateral strain only amounted to -0.6% (cf. Figure 6). For the critical thickness, Equation (2) revealed a value of 3.5 nm. All prepared NiO films were well above the critical thickness. Thus, the observed strong strain relaxation seems to be reasonable although they were not completely relaxed. We assume that the residual strain cannot be removed from the film due to kinetic barriers preventing the film from relaxing completely. Similar strain behavior was reported by Zhang et al. for NiO films of 2 nm thickness grown by pulsed laser deposition on SrTiO<sub>3</sub> substrates. In contrast to our findings, a complete relaxation for NiO films of thicknesses above 10 nm was observed, probably driven by higher deposition temperature [40].

In the case of Fe<sub>3</sub>O<sub>4</sub> on NiO/MgO, we calculated a vertical layer distance for a fully strained film of 2.092 Å and a critical thickness of 105 nm ( $\nu = 0.356$  [67],  $f = 0.3\%$ ), applying Equations (1) and (2), respectively. Here, the misfit  $f$  coincided with the misfit of magnetite on MgO since the growth of NiO on MgO was pseudomorphic adapting its lateral lattice constant (cf. Figure 6). All our investigated magnetite films on NiO/MgO were strongly strained, having a lower vertical layer distance than

received by Equation (1). Further, the calculated lateral layer distance of all prepared  $\text{Fe}_3\text{O}_4$  films was larger than that of the NiO films pseudomorphically grown on MgO (cf. Figure 6). Consequently, the magnetite films were exposed to much higher tensile lateral strain as expected from classical growth theory. This effect may be attributed to the unpreventable formation of APBs, which is not considered in the simple theories of epitaxial growth and relaxation via misfit dislocations. Thus, we assume that APBs expose additional tensile strain to the magnetite film. This result is in contrast to the compressive strain due to APBs as reported for magnetite films (thickness range 85–600 nm) directly grown on MgO(001) by magnetron sputtering [68]. As shown in Figure 4c, the measured vertical layer distance approached the bulk value with increasing  $\text{Fe}_3\text{O}_4$  thickness. However, the bulk value was not reached even for the thickest magnetite film on NiO/MgO studied here. On one hand, this effect is very surprising since the predicted critical thickness of 105 nm is beyond the thicknesses under consideration here. On the other hand, this behavior of partial relaxation below the calculated critical thickness also coincides with the results reported by Schemme et al. [33]. We also attribute this effect to the unpreventable formation of APBs, which is not considered in the simple theories for the nucleation of misfit dislocations. Thus, APBs seem to lower the kinetic barrier for the formation of dislocations.

Regardless of the low remaining compressive strain between the  $\text{Fe}_3\text{O}_4$  and NiO/SrTiO<sub>3</sub>, these magnetite films were less structurally ordered than the magnetite films grown on NiO/MgO. While the crystalline quality of the NiO films on SrTiO<sub>3</sub> was constantly high independent of the film thickness, the strength of Laue oscillations of the  $\text{Fe}_3\text{O}_4$  films grown on top of NiO/SrTiO<sub>3</sub> decreased with increasing magnetite thickness. This result is supported by the high surface roughness of the magnetite films obtained from the XRR measurements as well as by the broadened diffraction spots seen in the LEED pattern.

Assuming the pseudomorphic growth of magnetite on the strained NiO film with remaining lattice mismatch of  $-1\%$ , the vertical layer distance of a fully strained magnetite film was calculated to be  $2.123 \text{ \AA}$  using Equation (1). The measured value of  $2.117 \text{ \AA}$  for the 5 nm-thick magnetite film was already lower than the expected value for pseudomorphic growth (cf. Figure 4c). Thus, this magnetite film was already partially relaxed and showed vertical and lateral strain of  $0.9\%$  and  $0.8\%$ , respectively (cf. Figure 6). With increasing thickness of the magnetite film, the vertical and lateral layer distances strongly relaxed further to  $2.104 \text{ \AA}$  and  $2.093 \text{ \AA}$ , respectively, for the 20.7 nm-thick film. Again, this effect contradicts classical relaxation theory via dislocation formation from which the critical film thickness of 27 nm was obtained using Equation (2). Consequently, the formation of grain boundaries and structural defects (e.g., APBs) during the initial stage of film growth may support the formation of misfit dislocations, and thus a faster relaxation process. In addition, as stated above, the lateral tensile strain due to APBs may cause a larger lateral layer distance compared to pseudomorphic growth on the strained NiO film.

VSM measurements of the two thickest magnetite films on NiO/MgO and NiO/SrTiO<sub>3</sub> revealed ferro(i)magnetic behavior for both samples. However, the  $\text{Fe}_3\text{O}_4$  film grown on NiO/SrTiO<sub>3</sub> showed enhanced coercive field compared to the film on NiO/MgO, possibly caused by a higher density of grain boundaries, and thus the formation of more pinning centers as confirmed by the LEED analysis. This behavior coincides with the weaker structural ordering and higher surface roughness of the magnetite films on NiO/SrTiO<sub>3</sub>, also seen in the XRD and XRR measurements. An increased coercive field for magnetite films grown on SrTiO<sub>3</sub> caused by a higher surface roughness or strain has also been reported in Refs. [69,70].

The obtained saturation magnetization values of  $\text{Fe}_3\text{O}_4$  grown on NiO/MgO and NiO/SrTiO<sub>3</sub> coincided within the error tolerances with the values determined by XMCD [42]. Additionally, the value of  $\text{Fe}_3\text{O}_4$  film on NiO/MgO was also rather close to the ideal theoretical value as well as to the experimental bulk moment of magnetite of  $4.07 \mu_B/\text{f.u.}$  [5,63,71], whereas  $\text{Fe}_3\text{O}_4$  on NiO/SrTiO<sub>3</sub> exhibited a lower value. A reduced magnetic moment has also been reported for  $\text{Fe}_3\text{O}_4/\text{SrTiO}_3$  systems, possibly caused by a large density of APBs induced by high lattice mismatch [34,72]. This result is

supported by a weaker structural ordering as well as higher coercive fields and, thus, a higher density of grain boundaries observed for Fe<sub>3</sub>O<sub>4</sub> on NiO/SrTiO<sub>3</sub>.

Further, both investigated samples showed a fourfold magnetic in-plane anisotropy with magnetic easy axes aligned along the  $\langle 100 \rangle$  directions. For thin magnetite films on MgO(001), the magnetic easy axes are mostly reported to point into  $\langle 110 \rangle$  directions [70,73,74] as expected from bulk properties of Fe<sub>3</sub>O<sub>4</sub>. However, a magnetic isotropic behavior [74,75] or magnetic easy axes aligned in  $\langle 100 \rangle$  directions [76] are also presented in the literature for Fe<sub>3</sub>O<sub>4</sub>/MgO(001). Moreover, magnetite films grown on an iron buffer layer deposited on MgO(001) also exhibited a magnetic in-plane anisotropy with magnetic easy axes parallel to  $\langle 100 \rangle$  [77]. For Fe<sub>3</sub>O<sub>4</sub> films on SrTiO<sub>3</sub>(001), different orientations of the magnetic easy axes were also reported. While Kale et al. observed a fourfold magnetic anisotropy with magnetic easy axes pointing into  $\langle 110 \rangle$  directions [75], magnetic easy axes aligned along the  $\langle 100 \rangle$  directions are presented in Refs. [35,76]. All these observations show that the magnetic properties of magnetite are highly affected by the interface between the film and substrate and can be influenced by the deposition conditions, lattice mismatch, or stoichiometric deviations. In addition, we assume that a tetragonal distortion of the films can influence the spin–orbit coupling, which may lead to modified magnetocrystalline anisotropy constants [78] and, thus, altered directions of magnetic easy and hard axes.

## 5. Conclusions

We present a comparative study on the structural and magnetic properties of Fe<sub>3</sub>O<sub>4</sub>/NiO bilayers grown on MgO(001) and Nb-doped SrTiO<sub>3</sub>(001). Stoichiometric magnetite and NiO films with homogenous thicknesses were found on both substrates in the investigated thickness range (5–20 nm). Detailed analysis of the XRD measurements revealed a high crystallinity of the NiO films independent of the underlying substrate or film thickness. However, magnetite films grown on NiO/SrTiO<sub>3</sub> showed a weaker structural ordering and higher surface roughness compared to the films grown on NiO/MgO, induced by a large lattice mismatch and the resulting relaxation process. Further, the bilayers exhibited a vertical compressive strain on MgO but a tensile strain in the vertical direction on SrTiO<sub>3</sub> as a result of lateral compression. The weaker crystalline structure of Fe<sub>3</sub>O<sub>4</sub> on NiO/SrTiO<sub>3</sub> affected the magnetic properties, leading to an enhanced coercive field and a reduced magnetic moment compared to magnetite on NiO/MgO. Nevertheless, these Fe<sub>3</sub>O<sub>4</sub>/NiO bilayers on MgO and SrTiO<sub>3</sub> substrates are expected to show large thermoelectric effects based on the thermal generation of spin currents (spin Seebeck effect) [11–13], supported by the antiferromagnetic NiO layer [21,22].

Additionally, both systems showed a fourfold magnetic in-plane anisotropy with magnetic easy axes pointing in  $\langle 100 \rangle$  directions which were 45° rotated to the well-known magnetic easy axes directions of thin magnetite films on MgO(001) as expected from bulk properties. One potential reason may be a modified spin–orbit coupling as a result of the tetragonal distortion of the films leading to altered magnetocrystalline anisotropy. A detailed understanding of these bilayers is of the utmost importance since they are excellent candidates for potential spintronic and spin caloritronic applications. Therefore, this behavior deserves further study to shed more light on this interesting change of the magnetic anisotropy of Fe<sub>3</sub>O<sub>4</sub> thin films grown on NiO/MgO(001) and NiO/SrTiO<sub>3</sub>(001).

**Author Contributions:** Conceptualization, J.W., K.K., O.K.; Formal Analysis, O.K., T.S., T.K.; Investigation, O.K., N.P., K.R., J.R., T.K., J.W.; Data Curation, O.K.; Software, F.B.; Writing—Original Draft Preparation, O.K.; Writing—Review & Editing, J.W.; Supervision, J.W., K.K.; Project Administration, J.W.; Funding Acquisition, K.K.

**Funding:** This research was funded by the Deutsche Forschungsgemeinschaft (DFG) grant number [KU2321/2-1] and [KU3271/1-1].

**Acknowledgments:** Portions of this research were carried out at beamline I811, MaXLab synchrotron radiation source, Lund University, Sweden. Funding for the beamline I811 project was kindly provided by The Swedish Research Council and The Knut och Alice Wallenbergs Stiftelse. Additional experiments were performed at the X04SA beamline at the Swiss Light Source synchrotron radiation source at Paul Scherrer Institute, Villigen, Switzerland. We like to thank the I811 and X04SA beamline staff for experimental support. Further,

we acknowledge support by Deutsche Forschungsgemeinschaft (DFG) and Open Access Publishing Fund of Osnabrück University.

**Conflicts of Interest:** The authors declare no conflict of interest. The founding sponsors had no role in the design of the study; in the collection, analyses, or interpretation of data; in the writing of the manuscript, and in the decision to publish the results.

## References

1. Rao, C.N.R. Transition metal oxides. *Annu. Rev. Phys. Chem.* **1989**, *40*, 291–326. [[CrossRef](#)]
2. Hoffmann, A.; Bader, S.D. Opportunities at the frontiers of spintronics. *Phys. Rev. Appl.* **2015**, *4*, 047001. [[CrossRef](#)]
3. Bauer, G.E.W.; Saitoh, E.; van Wees, B.J. Spin caloritronics. *Nat. Mater.* **2012**, *11*, 391–399. [[CrossRef](#)] [[PubMed](#)]
4. Moussy, J.B. From epitaxial growth of ferrite thin films to spin-polarized tunnelling. *J. Phys. D Appl. Phys.* **2013**, *46*, 143001. [[CrossRef](#)]
5. Zhang, Z.; Satpathy, S. Electron states, magnetism, and the Verwey transition in magnetite. *Phys. Rev. B* **1991**, *44*, 13319–13331. [[CrossRef](#)]
6. Cornell, R.; Schwertmann, U. *The Iron Oxides: Structure, Properties, Reactions, Occurrences and Uses*; Wiley-VCH GmbH & Co. KGaA: Weinheim, Germany, 2004.
7. Seneor, P.; Fert, A.; Maurice, J.L.; Montaigne, F.; Petroff, F.; Vaurés, A. Large magnetoresistance in tunnel junctions with an iron oxide electrode. *Appl. Phys. Lett.* **1999**, *74*. [[CrossRef](#)]
8. Kado, T. Large room-temperature inverse magnetoresistance in tunnel junctions with a Fe<sub>3</sub>O<sub>4</sub> electrode. *Appl. Phys. Lett.* **2008**, *92*, 092502. [[CrossRef](#)]
9. Marnitz, L.; Rott, K.; Niehörster, S.; Klewe, C.; Meier, D.; Fabretti, S.; Witziok, M.; Krampf, A.; Kuschel, O.; Schemme, T.; et al. Sign change in the tunnel magnetoresistance of Fe<sub>3</sub>O<sub>4</sub>/MgO/Co-Fe-B magnetic tunnel junctions depending on the annealing temperature and the interface treatment. *AIP Adv.* **2015**, *5*, 047103. [[CrossRef](#)]
10. Wada, E.; Watanabe, K.; Shirahata, Y.; Itoh, M.; Yamaguchi, M.; Taniyama, T. Efficient spin injection into GaAs quantum well across Fe<sub>3</sub>O<sub>4</sub> spin filter. *Appl. Phys. Lett.* **2010**, *96*, 102510. [[CrossRef](#)]
11. Ramos, R.; Anadón, A.; Lucas, I.; Uchida, K.; Algarabel, P.A.; Morellón, L.; Aguirre, M.H.; Saitoh, E.; Ibarra, M.R. Thermoelectric performance of spin Seebeck effect in Fe<sub>3</sub>O<sub>4</sub>/Pt-based thin film heterostructures. *APL Mater.* **2016**, *4*, 104802. [[CrossRef](#)]
12. Ramos, R.; Kikkawa, T.; Uchida, K.; Adachi, H.; Lucas, I.; Aguirre, M.H.; Algarabel, P.; Morellón, L.; Maekawa, S.; Saitoh, E.; et al. Observation of the spin Seebeck effect in epitaxial Fe<sub>3</sub>O<sub>4</sub> thin films. *Appl. Phys. Lett.* **2013**, *102*, 072413. [[CrossRef](#)]
13. Uchida, K.I.; Adachi, H.; Kikkawa, T.; Kirihara, A.; Ishida, M.; Yoroazu, S.; Maekawa, S.; Saitoh, E. Thermoelectric generation based on spin Seebeck effects. *Proc. IEEE* **2016**, *104*, 1946–1973. [[CrossRef](#)]
14. Verwey, E.J.W. Electronic conduction of magnetite (Fe<sub>3</sub>O<sub>4</sub>) and its transition point at low temperatures. *Nature* **1939**, *144*, 327–328. [[CrossRef](#)]
15. Yoshida, J.; Iida, S. X-ray diffraction study on the low temperature phase of magnetite. *J. Phys. Soc. Jpn.* **1977**, *42*, 230–237. [[CrossRef](#)]
16. Kato, K.; Iida, S. Observation of ferroelectric hysteresis loop of Fe<sub>3</sub>O<sub>4</sub> at 4.2 K. *J. Phys. Soc. Jpn.* **1982**, *51*, 1335–1336. [[CrossRef](#)]
17. Alexe, M.; Ziese, M.; Hesse, D.; Esquinazi, P.; Yamauchi, K.; Fukushima, T.; Picozzi, S.; G'osele, U. Ferroelectric switching in multiferroic magnetite (Fe<sub>3</sub>O<sub>4</sub>) thin films. *Adv. Mater.* **2009**, *21*, 4452. [[CrossRef](#)]
18. Meiklejohn, W.H.; Bean, C.P. New Magnetic Anisotropy. *Phys. Rev.* **1956**, *102*, 1413–1414. [[CrossRef](#)]
19. Srinivasan, G.; Seehra, M.S. Magnetic susceptibilities, their temperature variation, and exchange constants of NiO. *Phys. Rev. B* **1984**, *29*, 6295. [[CrossRef](#)]
20. James, M.; Hibma, T. Thickness-dependent relaxation of NiO(001) overlayers on MgO(001) studied by x-ray diffraction. *Surf. Sci.* **1999**, *433–435*, 718–722. [[CrossRef](#)] [[PubMed](#)]
21. Lin, W.; Chen, K.; Zhang, S.; Chien, C.L. Enhancement of thermally injected spin current through an antiferromagnetic insulator. *Phys. Rev. Lett.* **2016**, *116*, 186601. [[CrossRef](#)]

22. Prakash, A.; Brangham, J.; Yang, F.; Heremans, J.P. Spin Seebeck effect through antiferromagnetic NiO. *Phys. Rev. B* **2016**, *94*, 014427. [[CrossRef](#)]
23. Hashimoto, S.; Peng, J.L.; Gibson, W.; Schowalter, L.J.; Fathauer, R.W. Strain measurement of epitaxial CaF<sub>2</sub> on Si (111) by MeV ion channeling. *Appl. Phys. Lett.* **1985**, *47*. [[CrossRef](#)]
24. Holanda, J.; Maior, D.S.; Santos, O.A.; Vilela-Leão, L.H.; Mendes, J.B.S.; Azevedo, A.; Rodríguez-Suárez, R.L.; Rezende, S.M. Spin-current to charge-current conversion and magnetoresistance in a hybrid structure of graphene and yttrium iron garnet. *Appl. Phys. Lett.* **2017**, *111*, 172405. [[CrossRef](#)]
25. Hoozeboom, G.R.; Aqeel, A.; Kuschel, T.; Palstra, T.T.M.; van Wees, B.J. Negative spin Hall magnetoresistance of Pt on the bulk easy-plane antiferromagnet NiO. *Appl. Phys. Lett.* **2017**, *111*, 052409. [[CrossRef](#)] [[PubMed](#)]
26. Hou, D.; Qui, Z.; Barker, J.; Sato, K.; Yamamoto, K.; Vélez, S.; Gomez-Perez, J.M.; Hueso, L.E.; Casanova, F.; Saitoh, E. Tunable sign change of spin Hall magnetoresistance in Pt=NiO=YIG structures. *Phys. Rev. Lett.* **2017**, *118*, 147202. [[CrossRef](#)]
27. Bertram, F.; Deiter, C.; Schemme, T.; Jentsch, S.; Wollschläger, J. Reordering between tetrahedral and octahedral sites in ultrathin magnetite films grown on MgO(001). *J. Appl. Phys.* **2013**, *113*, 184103. [[CrossRef](#)]
28. Arora, S.K.; Wu, H.C.; Choudhary, R.J.; Shvets, I.V.; Mryasov, O.N.; Yao, H.; Ching, W.Y. Giant magnetic moment in epitaxial Fe<sub>3</sub>O<sub>4</sub> thin films on MgO(100). *Phys. Rev. B* **2008**, *77*, 134443. [[CrossRef](#)]
29. Arora, S.K.; Sofin, R.G.S.; Shvets, I.V.; Luysberg, M. Anomalous strain relaxation behavior of Fe<sub>3</sub>O<sub>4</sub>/MgO(100) heteroepitaxial system grown using molecular beam epitaxy. *J. Appl. Phys.* **2006**, *100*, 073908. [[CrossRef](#)]
30. Wu, H.C.; Ramos, R.; Sofin, R.G.S.; Liao, Z.M.; Abid, M.; Shvets, I.V. Transversal magneto-resistance in epitaxial Fe<sub>3</sub>O<sub>4</sub> and Fe<sub>3</sub>O<sub>4</sub>/NiO exchange biased system. *Appl. Phys. Lett.* **2012**, *101*, 052402. [[CrossRef](#)]
31. Gatel, C.; Snoeck, E.; Serin, V.; Fert, A.R. Epitaxial growth and magnetic exchange anisotropy in Fe<sub>3</sub>O<sub>4</sub>/NiO bilayers grown on MgO(001) and Al<sub>2</sub>O<sub>3</sub>(0001). *Eur. J. Phys. B* **2005**, *45*. [[CrossRef](#)]
32. Wu, H.C.; Arora, S.K.; Mryasov, O.N.; Shvets, I.V. Antiferromagnetic interlayer exchange coupling between Fe<sub>3</sub>O<sub>4</sub> layers across a nonmagnetic MgO dielectric layer. *Appl. Phys. Lett.* **2008**, *92*, 182502. [[CrossRef](#)]
33. Schemme, T.; Kuschel, O.; Bertram, F.; Kuepper, K.; Wollschläger, J. Structure and morphology of epitaxially grown Fe<sub>3</sub>O<sub>4</sub>/NiO bilayers on MgO(001). *Thin Solid Films* **2015**, *589*, 526–533. [[CrossRef](#)]
34. Chen, Y.Z.; Sun, J.R.; Han, Y.N.; Xie, X.Y.; Shen, J.; Rong, C.B.; He, S.L.; Shen, B.G. Microstructure and magnetic properties of strained Fe<sub>3</sub>O<sub>4</sub> films. *J. Appl. Phys.* **2008**, *103*, 07D703. [[CrossRef](#)]
35. Monti, M.; Sanz, M.; Oujja, M.; Rebollar, E.; Castillejo, M.; Pedrosa, F.J.; Bollero, A.; Camarero, J.; Cunado, J.L.F.; Nemes, N.M.; et al. Room temperature in-plane <100> magnetic easy axis for Fe<sub>3</sub>O<sub>4</sub>/SrTiO<sub>3</sub>(001):Nb grown by infrared pulsed laser deposition. *J. Appl. Phys.* **2013**, *114*, 223902. [[CrossRef](#)]
36. Liu, X.H.; Liu, W.; Zhang, Z.D. Evolution of magnetic properties in the vicinity of the Verwey transition in Fe<sub>3</sub>O<sub>4</sub> thin films. *Phys. Rev. B* **2017**, *96*, 094405. [[CrossRef](#)]
37. Kuschel, O.; Buß, R.; Spiess, W.; Schemme, T.; Wöllermann, J.; Balinski, K.; N'Diaye, A.T.; Kuschel, T.; Wollschläger, J.; Kuepper, K. From Fe<sub>3</sub>O<sub>4</sub>/NiO bilayers to NiFe<sub>2</sub>O<sub>4</sub>-like thin films through Ni interdiffusion. *Phys. Rev. B* **2016**, *94*, 094423. [[CrossRef](#)]
38. Chern, G.; Cheng, C. Interface matching in oxides of rocksalt/rocksalt(001) and rocksalt/perovskite(001). *J. Vac. Sci. Technol.* **1999**, *A17*. [[CrossRef](#)]
39. Kennedy, R.J. The growth of iron oxide, nickel oxide and cobalt oxide thin films by laser ablation from metal targets. *IEEE Trans. Magn.* **1995**, *31*, 3829–3831. [[CrossRef](#)] [[PubMed](#)]
40. Zhang, K.H.L.; Wu, R.; Tang, F.; Li, W.; Oropeza, R.E.; Qiao, L.; Lazarov, V.K.; Du, Y.; Payne, D.J.; MacManus-Driscoll, J.L.; et al. Electronic structure and band alignment at the NiO and SrTiO<sub>3</sub> p-n heterojunctions. *Appl. Mater. Interfaces* **2017**, *9*, 26549–26555. [[CrossRef](#)]
41. Pilard, M.; Ersen, O.; Cherifi, S.; Carvello, B.; Roiban, L.; Muller, B.; Scheurer, F.; Ranno, L.; Boeglin, C. Magnetic properties of coupled ultrathin NiO/Fe<sub>3</sub>O<sub>4</sub> (001) films. *Phys. Rev. B* **2007**, *76*, 214436. [[CrossRef](#)]
42. Kuepper, K.; Kuschel, O.; Pathé, N.; Schemme, T.; Schmalhorst, J.; Thomas, A.; Arenholz, E.; Gorgoi, M.; Ovsyannikov, R.; Bartkowski, S.; et al. Electronic and magnetic structure of epitaxial Fe<sub>3</sub>O<sub>4</sub>(001)/NiO heterostructures grown on MgO(001) and Nb-doped SrTiO<sub>3</sub>(001). *Phys. Rev. B* **2016**, *94*, 024401. [[CrossRef](#)]

43. Krug, I.P.; Hillebrecht, F.U.; Haverkort, M.W.; Tanaka, A.; Tjeng, L.H.; Gomonay, H.; Fraile-Rodriguez, A.; Nolting, F.; Cramm, S.; Schneider, C.M. Impact of interface orientation on magnetic coupling in highly ordered systems: A case study of the low-indexed Fe<sub>3</sub>O<sub>4</sub>/NiO interfaces. *Phys. Rev. B* **2008**, *78*, 064427. [[CrossRef](#)]
44. Wang, H.Q.; Gao, W.; Altman, E.I.; Heinrich, V.E. Studies of the electronic structure at the Fe<sub>3</sub>O<sub>4</sub>-NiO interface. *J. Vac. Sci. Technol. A* **2004**, *22*. [[CrossRef](#)]
45. Parratt, L. Surface studies of solids by total reflection of x-rays. *Rev. Mod. Phys.* **1954**, *95*. [[CrossRef](#)]
46. Névot, L.; Croce, P. Caractérisation des surfaces par réflexion rasante de rayons X. Application à l'étude du polissage de quelques verres silicates. *Rev. Phys. Appl.* **1980**, *15*, 761–779.
47. Als-Nielsen, J.; McMorrow, D. *Elements of Modern X-Ray Physics*; John Wiley & Sons, Ltd.: Hoboken, NJ, USA, 2001. [[CrossRef](#)]
48. Henzler, M. Measurement of surface defects by low-energy electron diffraction. *Appl. Phys. A* **1984**, *34*, 205–214. [[CrossRef](#)]
49. Pentcheva, R.; Moritz, W.; Rundgren, J.; Frank, S.; Schrupp, D.; Scheffler, M. A combined DFT/LEED-approach for complex oxide surface structure determination: Fe<sub>3</sub>O<sub>4</sub>(001). *Surf. Sci.* **2008**, *602*, 1299–1305. [[CrossRef](#)]
50. Korecki, J.; Handke, B.; Spiridis, N.; Slezak, T.; Flis-Kabulska, F.; Haber, J. Size effects in epitaxial films of magnetite. *Thin Solid Films* **2002**, *412*, 14–23. [[CrossRef](#)]
51. Anderson, J.F.; Kuhn, M.; Diebold, U.; Shaw, K.; Stoyanov, P.; Lind, D. Surface structure and morphology of Mg-segregated epitaxial Fe<sub>3</sub>O<sub>4</sub>(001) thin films on MgO(001). *Phys. Rev. B* **1997**, *56*. [[CrossRef](#)] [[PubMed](#)]
52. Bliem, R.; McDermott, E.; Ferstl, P.; Setvin, M.; Gamba, O.; Pavelec, J.; Schneider, M.A.; Schmid, M.; Diebold, U.; Blaha, P.; et al. Subsurface cation vacancy stabilization of the magnetite (001) surface. *Science* **2014**, *346*, 1215–1218. [[CrossRef](#)]
53. Nesbitt, H.; Legrand, D.; Bancroft, G. Interpretation of Ni2p XPS spectra of Ni conductors and Ni insulators. *Phys. Chem. Miner.* **2000**, *27*, 357–366. [[CrossRef](#)]
54. Grosvenor, A.P.; Biesinger, M.C.; Smart, R.S.C.; McIntyre, N.S. New interpretations of XPS spectra of nickel metal and oxides. *Surf. Sci.* **2006**, *600*, 1771–1779. [[CrossRef](#)]
55. Uhlenbrock, S.; Scharfschwerdtt, C.; Neumann, M.; Illing, G.; Freund, H.J. The influence of defects on the Ni 2p and O 1s XPS of NiO. *J. Phys. Condens. Matter* **1992**, *4*, 7973–7978. [[CrossRef](#)]
56. Soriano, L.; Preda, I.; Gutiérrez, A.; Palacín, S.; Abbate, M.; Vollmer, A. Surface effects in the Ni 2p x-ray photoemission spectra of NiO. *Phys. Rev. B* **2007**, *75*, 233417. [[CrossRef](#)]
57. Mansour, A.N. Characterization of NiO by XPS. *Surf. Sci. Spectra* **1994**, *3*. [[CrossRef](#)]
58. Carley, A.; Jackson, S.; O'Shea, J.N.; Roberts, M.W. The formation and characterisation of Ni<sup>3+</sup>—An X-ray photoelectron spectroscopic investigation of potassium-doped Ni(110)-O. *Surf. Sci. Lett.* **1999**, *440*, L868–L874. [[CrossRef](#)]
59. Yamashita, T.; Hayes, P. Analysis of XPS spectra of Fe<sup>2+</sup> and Fe<sup>3+</sup> ions in oxide materials. *Appl. Surf. Sci.* **2008**, *254*, 2441–2449. [[CrossRef](#)]
60. Fujii, T.; de Groot, F.M.F.; Sawatzky, G.A.; Voogt, F.C.; Hibma, T.; Okada, K. In situ XPS analysis of various iron oxide films grown by NO<sub>2</sub>-assisted molecular-beam epitaxy. *Phys. Rev. B* **1999**, *59*. [[CrossRef](#)]
61. Henke, B.; Gullikson, E.; Davis, J. X-ray interactions: Photoabsorption, scattering, transmission, and reflection at E = 50–30000 eV, Z = 1–92. *At. Data Nucl. Data* **1993**, *54*, 181–342. [[CrossRef](#)]
62. Pimpinelli, A.; Villain, J. *Physics of Crystal Growth*; Cambridge University Press: Cambridge, UK, 1998. [[CrossRef](#)]
63. Jeng, H.T.; Guo, G.Y. First-principles investigations of the electronic structure and magnetocrystalline anisotropy in strained magnetite Fe<sub>3</sub>O<sub>4</sub>. *Phys. Rev. B* **2002**, *65*, 094429. [[CrossRef](#)]
64. Margulies, D.T.; Parker, F.T.; Rudee, M.L.; Spada, F.E.; Chapman, J.N.; Aitchison, P.R.; Berkowitz, A.E. Origin of the anomalous magnetic behavior in single crystal Fe<sub>3</sub>O<sub>4</sub> films. *Phys. Rev. Lett.* **1997**, *79*. [[CrossRef](#)]
65. Fleischer, K.; Mauit, O.; Shvets, I.V. Stability and capping of magnetite ultra-thin films. *Appl. Phys. Lett.* **2014**, *104*, 192401. [[CrossRef](#)]
66. Matthews, J.W.; Blakeslee, A.E. Defects in epitaxial multilayers: I. Misfit dislocations. *J. Cryst. Growth* **1974**, *27*, 118–125. [[CrossRef](#)]
67. Every, A.G.; McCurdy, A.K. *Table 7, Cubic System. Binary Compounds*; Springer Materials—The Landolt-Boernstein Database; Springer: Berlin/Heidelberg, Germany, 1992. [[CrossRef](#)]

68. Balakrishnan, K.; Arora, S.K.; Shvets, I.V. Strain relaxation studies of the Fe<sub>3</sub>O<sub>4</sub>/MgO(100) heteroepitaxial system grown by magnetron sputtering. *J. Phys. Condens. Matter* **2004**, *16*. [[CrossRef](#)]
69. Cheng, J.; Sterbinsky, G.E.; Wessels, B.W. Magnetic and magneto-optical properties of heteroepitaxial magnetite thin films. *J. Cryst. Growth* **2008**, *310*, 3730–3734. [[CrossRef](#)]
70. Dho, J.; Kim, B.; Ki, S. Substrate effects on in-plane magnetic anisotropy and Verwey transition temperatures of (100) magnetite (Fe<sub>3</sub>O<sub>4</sub>) films. *IEEE Trans. Magn.* **2016**, *52*, 2600304. [[CrossRef](#)]
71. Weiss, P.; Forrer, R. The absolute saturation of ferromagnetic and laws of approach according to the field and the temperature. *Ann. Phys.* **1929**, *10*, 279–372. [[CrossRef](#)]
72. Leung, G.W.; Vickers, M.E.; Yu, R.; Blamire, M.G. Epitaxial growth of Fe<sub>3</sub>O<sub>4</sub>(111) on SrTiO<sub>1</sub>(001) substrates. *J. Cryst. Growth* **2008**, *310*. [[CrossRef](#)]
73. Margulies, D.T.; Parker, F.T.; Berkowitz, A.E. Magnetic anomalies in single crystal Fe<sub>3</sub>O<sub>4</sub> thin films. *J. Appl. Phys.* **1994**, *75*. [[CrossRef](#)]
74. Schemme, T.; Pathé, N.; Niu, G.; Bertram, F.; Kuschel, T.; Kuepper, K.; Wollschläger, J. Magnetic anisotropy related to strain and thickness of ultrathin iron oxide films on MgO(001). *Mater. Res. Express* **2015**, *2*, 016101. [[CrossRef](#)]
75. Kale, S.; Bhagat, S.M.; Lofland, S.E.; Scabarozzi, T.; Ogale, S.B.; Orozco, A.; Shinde, S.R.; Venkatesan, T.; Hannover, B.; Mercey, B.; et al. Film thickness and temperature dependence of the magnetic properties of pulsed-laser-deposited Fe<sub>3</sub>O<sub>4</sub> films on different substrates. *Phys. Rev. B* **2001**, *64*, 205413. [[CrossRef](#)]
76. Prieto, P.; Prieto, J.E.; Gargallo-Caballero, R.; Marco, J.F.; de la Figueraca, J. Role of the substrate on the magnetic anisotropy of magnetite thin films grown by ion-assisted deposition. *Appl. Surf. Sci.* **2015**, *359*, 742–748. [[CrossRef](#)]
77. Schemme, T.; Krampf, A.; Bertram, F.; Kuschel, T.; Kuepper, K.; Wollschläger, J. Modifying magnetic properties of ultra-thin magnetite films by growth on Fe precovered MgO(001). *J. Appl. Phys.* **2015**, *118*, 113904. [[CrossRef](#)]
78. Wu, R.; Freeman, A.J. Spin-orbit induced magnetic phenomena in bulk metals and their surfaces and interfaces. *J. Magn. Magn. Mater* **1999**, *200*, 498–514. [[CrossRef](#)]



© 2018 by the authors. Licensee MDPI, Basel, Switzerland. This article is an open access article distributed under the terms and conditions of the Creative Commons Attribution (CC BY) license (<http://creativecommons.org/licenses/by/4.0/>).